



## Article

# Study of Initial $\beta$ -Zr Formation in $\beta$ -Quenched N36 Zirconium Alloy Using Dynamic and Metallographic Methods

Ali W. Aldeen <sup>1,2</sup>, Zhongwei Chen <sup>1,\*</sup>, Imad A. Disher <sup>3</sup>, Kang Yan <sup>1</sup> and Yongjia Zhu <sup>1</sup><sup>1</sup> State Key Laboratory of Solidification Processing, Northwestern Polytechnical University, Xi'an 710072, China<sup>2</sup> Department of Materials Engineering, College of Engineering, University of Kufa, Najaf 54001, Iraq<sup>3</sup> Department of Ceramics and Building Materials, College of Materials Engineering, University of Babylon, Hillah 51001, Iraq

\* Correspondence: chzw@nwpu.edu.cn; Tel./Fax: +86-29-88460253-8003

**Abstract:** In this study, the initial temperature of the ( $\alpha$ ) to ( $\alpha + \beta$ ) phase transformation of  $\beta$ -quenched N36 zirconium alloy was determined using differential scanning calorimetry (DSC) and metallographic techniques. Diagnosis and analysis of the difference between the two techniques were also conducted. It was found that the phase transition temperature, obtained by metallographic techniques, lies in a temperature range of 710–715 °C. This value is lower than that recorded by DSC analysis. A peak separation successfully explained the dissolution of the second phase particles (SPP)s and  $\alpha \rightarrow \beta$  phase transformation using the DSC analysis. Compared with previous studies, the results of this study showed that  $\beta$ -quenched starting material is responsible for the delay of  $\beta$ -Zr formation during the heat treatment of the N36 zirconium alloy.



**Citation:** Aldeen, A.W.; Chen, Z.; Disher, I.A.; Yan, K.; Zhu, Y. Study of Initial  $\beta$ -Zr Formation in  $\beta$ -Quenched N36 Zirconium Alloy Using Dynamic and Metallographic Methods. *Crystals* **2022**, *12*, 1535. <https://doi.org/10.3390/cryst12111535>

Academic Editors: Marek Sroka, Grzegorz Golański and Patrice Berthod

Received: 22 September 2022

Accepted: 25 October 2022

Published: 28 October 2022

**Publisher's Note:** MDPI stays neutral with regard to jurisdictional claims in published maps and institutional affiliations.



**Copyright:** © 2022 by the authors. Licensee MDPI, Basel, Switzerland. This article is an open access article distributed under the terms and conditions of the Creative Commons Attribution (CC BY) license (<https://creativecommons.org/licenses/by/4.0/>).

**Keywords:** N36 zirconium alloy; phase transformation; differential scanning calorimetry DSC; metallographic techniques

## 1. Introduction

Zirconium based alloys are commonly used in nuclear power reactors where they play an important role as fuel cladding or structural materials. Their adequate mechanical strength, low radiation absorption, high corrosion resistance, and fair performance stability made them the preferred candidate of choice in the selection of materials for such applications [1–5]. Based on this, many countries were involved in the development of modified or new zirconium alloys in order to improve their performance. For instance, to meet the escalating demands of fuel burn-up in pressurized water reactors (PWR), China developed N36 zirconium alloy based on the Zr-Nb and Zr-Sn series [1,6–8].

The manufacturing process of zirconium alloys involves several heat treatments and processing regimes. This is to ensure that the designed microstructure is protected and the desired properties are maintained; these are of great importance in order to keep the adequate behavior of these alloys in the most grueling imaginable circumstances [9–11]. During the manufacturing processes of fuel cladding materials, the materials go through a  $\beta$ -phase quenching process that produces a complex structure. Consequently, it is crucial to study and comprehend the role of the phase transformation in regulating the regimes of the manufacturing processes. Moreover, understanding the physical and chemical characteristics of the components in the core of the reactor is vital in relation to nuclear reactor safety [12,13].

Most of the investigations to determine the phase transition temperatures in zirconium alloys are carried out by using either dynamic or static techniques to produce reproducible results. Corresponding to the dynamic techniques, differential scanning calorimetry and differential thermal analysis (DTA) were employed, depending on the principles of dilatometry, electrical resistivity, and thermal analysis [14]. In static methods, on the other hand,

the study of  $\beta$ -Zr phase formation tends to be more intuitive, based on the principle of ‘what-you-see-is-what-you-get’.

In the past few decades, great efforts have been made with quaternary alloys to study the effect of the addition of different elements on the phase stability and transition temperature [15–17]. The effect of heating rates on the transformation temperature was also studied by many researchers [12,14,18–20]. Further, research was conducted to study the effect of irradiation on the phase transition temperature of these alloys [21–23].

These studies almost always started with a fully re-crystallized initial material. Hence, there is a lack of research work and information regarding the effect of the  $\beta$ -quenched state on the initial phase transition temperature, more specifically, in zirconium alloys having a dominant Nb, which is of high importance in the nuclear industry.

Therefore, this study aims to determine an accurate initial  $\beta$ -Zr formation that follows  $\beta$ -quenching treatment to specify the ( $\alpha$ ) to ( $\alpha + \beta$ ) transformation temperature in N36 zirconium alloy. Dynamic and metallographic methods were employed to gain an in-depth comprehension regarding this transformation.

## 2. Materials and Methods

The China Nuclear Institute supplied N36 zirconium alloy plate in a fully re-crystallized state with 1 mm thickness. The chemical composition of the supplied plate is presented in Table 1 as weight percent.

**Table 1.** Chemical composition of N36 zirconium alloy (wt.%).

Element	Sn	Nb	Fe	O	Zr
content	0.85	1	0.3	0.1	Bal.

Bal.-Balance other elements including Sn, Nb, Fe and O.

After cutting  $8 \times 6 \times 1 \text{ mm}^3$  from the original plate, the samples were placed in an evacuated glass tube at a pressure of  $4.7 \times 10^{-3} \text{ Pa}$  to prevent air oxidation during heat treatment, and subjected to  $\beta$ -solution treatment at  $1050 \text{ }^\circ\text{C}$  for 0.5 h. Then, the glass tube was transferred immediately from the furnace, and was broken down inside a vial of cold water to ensure rapid cooling.

For DSC analysis, a disc-shaped sample was machined from the  $\beta$ -quenched sample using a wire electrode cutting machine with 4 mm diameter and a weight of 55 mg; the disc was subjected to polishing and ultrasonic cleaning. The NETZSCH 449F system was used to analyze the N36 zirconium alloy under a controlled atmosphere. A thermal scan was done in a pure argon flow rate of 60 mL/min from an ambient temperature to  $1150 \text{ }^\circ\text{C}$  with a heating rate of  $5 \text{ }^\circ\text{C}/\text{min}$ . Peak separation software and Proteus thermal analysis software was used for the analysis of various enthalpy peaks of the DSC curve.

For the metallographic study, the  $\beta$ -quenched samples were sealed in an evacuated glass tubes and heated up to  $700 \text{ }^\circ\text{C}$ ,  $705 \text{ }^\circ\text{C}$ ,  $710 \text{ }^\circ\text{C}$ ,  $715 \text{ }^\circ\text{C}$  and  $720 \text{ }^\circ\text{C}$  for 1 h, followed by rapid quenching, in the same way described in the  $\beta$ -solution treatment, to ensure rapid cooling so that the integrity of the sample’s microstructure is maintained.

An optical microscope (OM) and back scattering electron (BSE) detector equipped on the FEI nova 400 field emission gun scanning electron microscopy (FEG-SEM) were used to acquire the microstructure of the  $\beta$ -quenched samples. FEG-SEM was used for the observation of surface morphology evolution. FEI Tecnai G2 F20 SuperTwin transmission electron microscopy (TEM), with an accelerating voltage of 200 Kv, was used to generate a bright-field (BF)-TEM image for the microstructure. An energy-dispersive spectroscopy (EDS) equipped within the TEM and selected area electron diffraction (SAED) were used for identification and the analyses phase structure.

Before any metallographic observation, the samples were subjected to mechanical ground by SiC papers up to 7000#. A solution of 45% deionized water, 45% nitric acid, and 10% perchloric acid was used as etching agent in the samples’ preparation for FEG-SEM by rubbing for 20 sec with cotton wool. For SEM-BSE, the surface was electro-polished at  $20 \text{ }^\circ\text{C}$

with 20 V as polishing voltage in a solution of 70% methanol, 20% ethylene glycol, and 10% perchloric acid. A solution of 90% ethanol and 10% perchloric acid with conventional twin-jet equipment was used for TEM samples preparation below  $-35\text{ }^{\circ}\text{C}$ .

Imaging software was used to calculate the fraction of the precipitates, as 2D images have been used, and the calculated fraction represents an area fraction. Statistical information of the precipitates was acquired for at least 350–500 particles for each samples; this process was repeated for at least three different images for each sample.

### 3. Results and Discussion

#### 3.1. Dynamic Technique

Figure 1 shows the microstructure of the  $\beta$ -quenched sample. From the OM image, shown in Figure 1a, shows that the microstructure consists of  $\alpha$ -plates are surrounded by prior  $\beta$ -grain boundaries, while the BSE image, shown in Figure 1b, shows that these plates have an interlaced structure of a fine plates that have an average thickness of about  $1\text{ }\mu\text{m}$ . Such fine, complex structure is believed to result from shear transformation, developed during the rapid cooling of the samples that had the matrix super saturated by alloying elements [24,25].

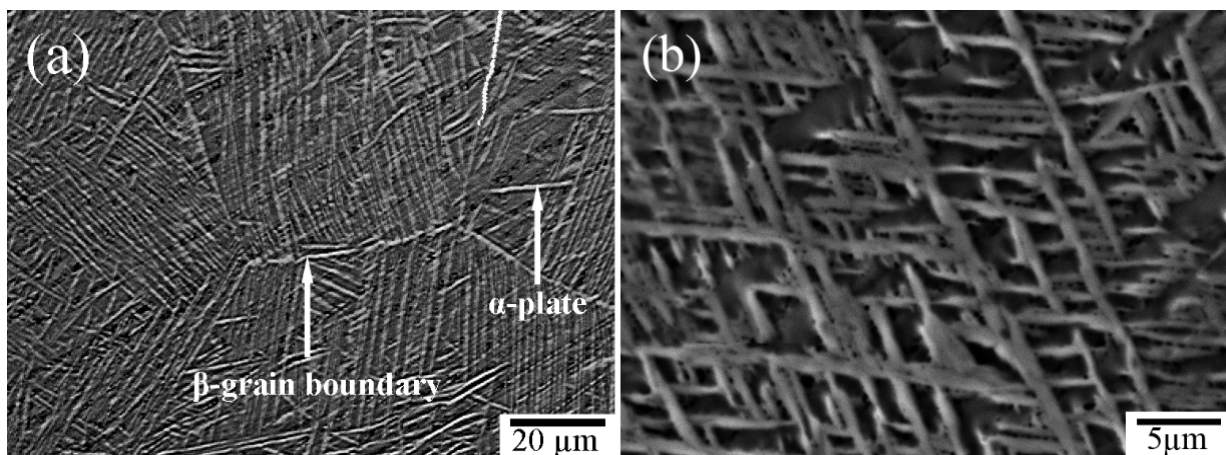


**Figure 1.**  $\beta$ -quenched microstructure: (a) OM image (b) BSE image.

The DSC curve of N36 zirconium alloy, evaluated by using Proteus thermal analysis software, is presented in Figure 2. Unlike the fully re-crystallized samples reported in previous studies, the thermograph starts with noisy peaks and indicates an exothermic process below  $700\text{ }^{\circ}\text{C}$ ; this possibly corresponds to structural relaxation of the as-quenched sample as reported by various studies on different materials [26–28]. The phase transition temperature  $T_{\alpha \rightarrow \alpha + \beta}$  is to be  $738.2\text{ }^{\circ}\text{C}$ ; this temperature was recorded during the warm-up process. Two endothermic peaks (S and T) could be observed between the onset and the offset positions of  $\alpha/\beta$  phase transition. Niculina et al. [23] reported that the overlap of the endothermic peaks could be attributed to both the SPPs dissolution and the  $\alpha \rightarrow \beta$  phase transformation during the heating process. Zhao et al. [18] determined that the initial temperature of the transformation from  $\alpha$  phase to  $\alpha + \beta$  phases, in a fully recrystallized starting state of N36 (Zr-1.0Sn-1.0Nb-0.3Fe) alloy, is  $725\text{ }^{\circ}\text{C}$ . The difference in the initial transition temperature for different alloys is related to the differences in their chemical composition. According to many studies [12,29,30], the  $T_{\alpha \rightarrow \alpha + \beta}$  transition temperature was found to increase with increasing Sn content in alloy. Therefore, Sn is known to be  $\alpha$ -stabilizer phase [25]. In this research, an Sn content of 0.85 wt.% was used; this percent is less than that used by Zhao, 1 wt.%, with equal chemical content of the remaining alloying elements in the two alloys. However, the phase transition temperature observed in the current study is higher than that reported by Zhao. Based on the difference in the Sn content between the two alloys, a lower transition temperature was expected or, at most, almost the same  $T_{\alpha \rightarrow \alpha + \beta}$  transition temperature, but not a higher temperature. Despite the non-

equilibrium conditions that lead to the phenomenon of thermal retardation, which we tried to reduce by using a slow heating rate, the higher transition temperature could be ascribed to the  $\beta$ -quenched starting state of the alloy in the current study; at that state, the alloy needs more energy and time to proceed re-crystallization and to push up the dislocations towards the grain boundaries where the nucleation of the new phases is expected; thus, the nucleation of the new phases acquired a higher temperature. In contrast, an alloy in the fully re-crystallized starting state is expected to facilitate the pathways for  $\beta$ -phase formation in its preferred sites at the grain boundaries.

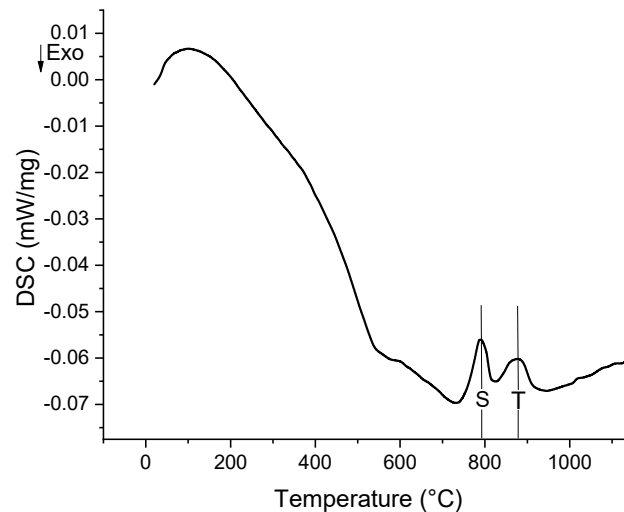


**Figure 2.** DSC curve of N36 zirconium alloy executed at constant heating rate of 5 °C/min.

Figure 3 shows that the low-temperature endothermic peak is semi-sharp. This result is not in full agreement with that observed by Qiu et al. [14] concerning Zr-1.0Sn-0.3Nb-0.3Fe alloy; they revealed that the low-temperature endothermic peak has a sharp shape, and they attributed that to the presence of a narrow temperature range for the SPPs dissolution process. In our previous study of SPPs growth kinetics calculation for samples similar for that of the current alloy [25], it was found that Nb participates in most SPPs and it plays a crucial role in slowing down the diffusion rate, causing high growth kinetics energy. Consequently, the same role was played by Nb in the slow dissolution process based on the atomic radii argument. Hence, instead of appearing sharp, the SPPs dissolution peak appears as semi-sharp. Table 2 lists the transition temperature for N36 zirconium alloy obtained by DSC results.

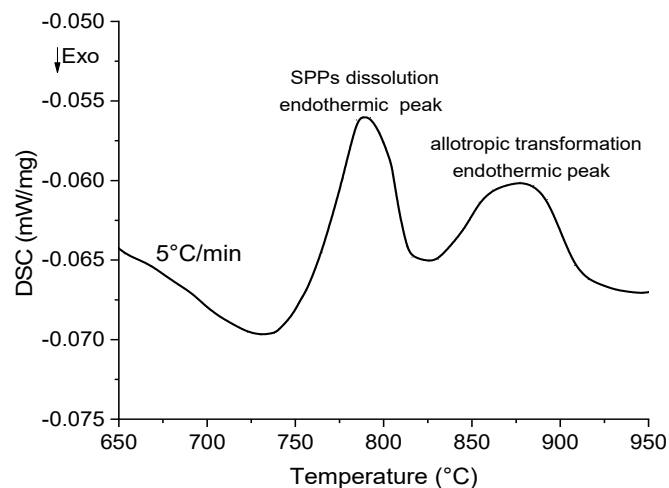


**Figure 3.** A peak separation result of two endothermic enthalpy peaks of N36 zirconium alloy DSC curve acquired at 5 °C/min.

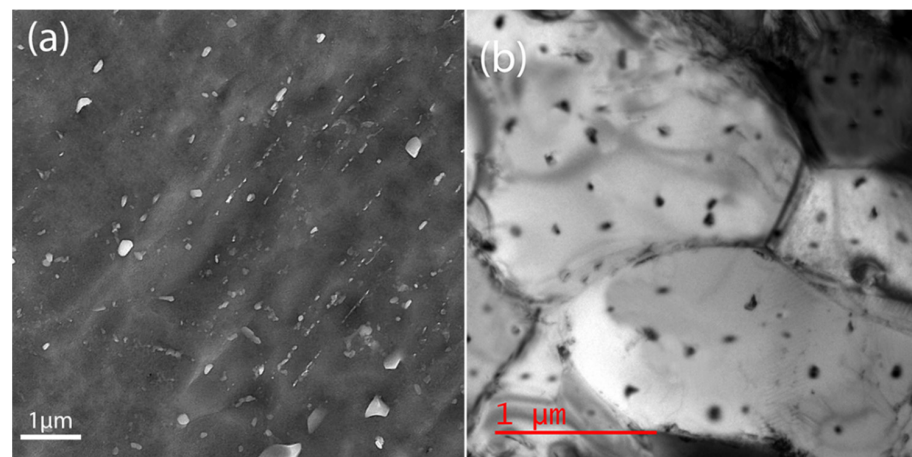


**Table 2.**  $\alpha$  to  $\alpha + \beta$  transition temperature and Peaking values of N36 zirconium alloy obtained by DSC measurement.

Heating Rate	$T_{\alpha \rightarrow \alpha + \beta}$ (°C)	Peaking Temperatures (°C)	
		SPPs Dissolution (S)	$\alpha/\beta$ Transition (T)
5	738.2	789.3	877.9

### 3.2. Metallographic Techniques

Previous studies [14,18,31] on the microstructure variation and phase transformation of zirconium alloys demonstrated that the  $\beta$ -Zr phase starts to form as triangular precipitates at grain boundaries or trigeminal grain boundaries; this transformation occurs when the sample heat was treated at a temperature close almost to the  $T_{\alpha \rightarrow \alpha + \beta}$  measured by the dynamic technique. However, Figure 4a,b, show that no triangular precipitates could be observed for sample heat treated at 700 °C, which is close to the  $T_{\alpha \rightarrow \alpha + \beta}$  of the DSC result and that specified by Zhao et al. [18] for a fully re-crystallized N36 alloy. The FEG-SEM image in Figure 4a confirms the presence of precipitates that distributed randomly with spherical, ellipsoidal, or irregular shapes. Correspondingly, the TEM image in Figure 4b shows the same types of precipitates that distributed randomly as well. Therefore, the two observations agree that there are not triangular precipitates. As a result, metallographic examination temperatures should be closer to the DSC result to find the phase transition temperature.

**Figure 4.** Quenched sample at 700 °C: (a) FEG-SEM image (b) TEM image.

For the samples heat treated and quenched at 705, 710, 715 and 720 °C, it is expected that samples cool swiftly, resulting in the shear phase transformation and the maintenance of the new phase in the matrix. Figure 5 shows the FEG-SEM results of these quenched samples. From Figure 5a,b, for samples heat treated at 705 °C and 710 °C, it is apparent that there are numerous SPPs with circular, elliptical and irregular precipitate shapes, in agreement with the result shown in Figure 4. Moreover, no triangle precipitates were observed at grain boundaries or trigeminal grain boundaries. Based on preliminary findings, these alloys did not go through a phase transition. In contrast, Figure 5c,d for samples heat treated and quenching at 715 °C and 720 °C, various triangular precipitates were noticed at grain boundaries and trigeminal grain boundaries, beside the spherical or ellipsoidal precipitates. Generally, it is accepted that a higher energy state, irregular atom arrangements, and a high dislocation density at the grain boundaries enable phase change nucleation at such locations. In a comparison between Figure 5c,d, it is only possible to see the triangular precipitates at a few trigeminal grain boundaries in Figure 5c. On the other hand, Figure 5d shows that there are numerous triangular precipitates with larger size. This is in consistent with the reality that rising temperatures lead to a similar rise in the area percentage of  $\beta$ -Zr

phase. Therefore, when a triangular phase is formed with small size in a sample aged at a specific temperature, this temperature can be determined as the phase transition initial point. Combine this result with that of the sample quenched at 710 °C, where no triangular phase was found, and the temperature of  $T_{\alpha \rightarrow \alpha + \beta}$  at which the N36 alloy goes through is estimated to be 710–715 °C.

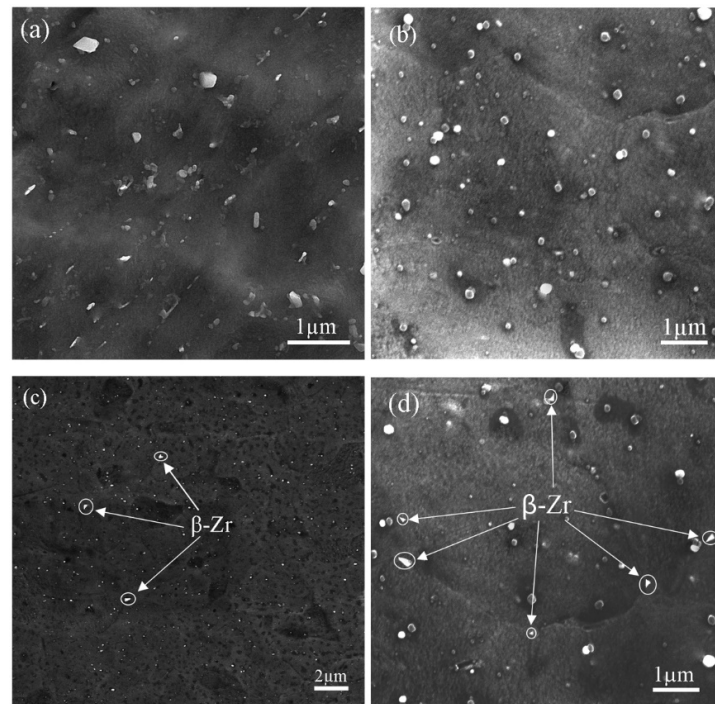


**Figure 5.** FEG-SEM images of different quenched samples: (a) at 705 °C (b) at 710 °C (c) at 715 °C (d) at 720 °C.

To confirm if the triangular phase in Figure 5c,d is  $\beta$ -Zr, Figure 6a–c shows the TEM image of the sample quenched at 715 °C and its corresponding SAED and EDS. In Figure 6a, the selected area, located within a red circle, has a body-centered cubic structure as can be seen from the pattern in Figure 6b with [1-1-1] zone axis. It is well known that zirconium alloys have two phases with body centered cubic crystal lattice, namely  $\beta$ -Nb and  $\beta$ -Zr. However, if the result of the SAED is looked at with the EDS result in Figure 6c, it becomes apparent that this phase has considerably low Fe content and high Zr content, in opposite to the Fe content in Zr-Nb-Fe SPPs which is relatively high [25], confirming that the triangular phase is  $\beta$ -Zr. Moreover, even though the cubic structure of  $\beta$ -Nb is a body-centered cubic structure, it is mainly composed of tiny circular particles instead of triangles, and the Nb element inside it is extremely high [32]. However, EDS analysis shows a relatively low Nb content.

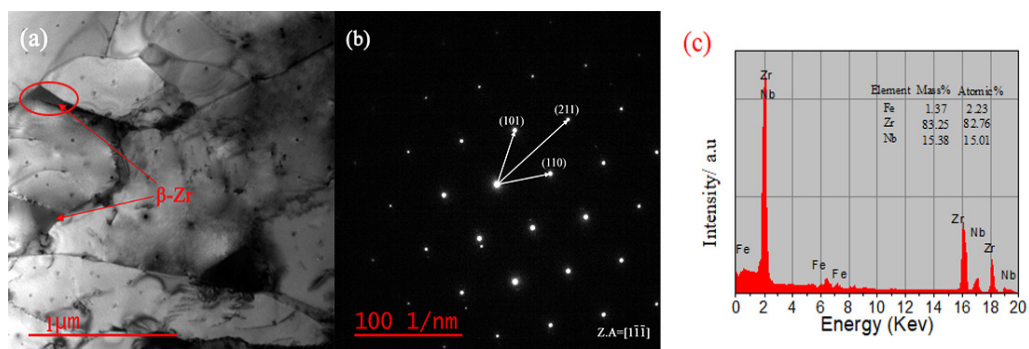


**Figure 6.** 715 °C quenched sample: (a) BF-TEM image (b) SAED (c) EDS.

Figure 7 represents the average area fraction and average precipitate size of  $\beta$ -Zr and other SPPs in respect to each aging temperature. The area fraction of SPPs is almost the same, with a slight decrease with increasing temperature, correspondingly, there is a decrease in the particles size of SPPs with increasing temperature, probably because of the dissolution process and prelude to phase transition process, while the area fraction of  $\beta$ -Zr sees little increase with increasing temperature after they appeared at 715 °C. In agreement, the size of  $\beta$ -Zr coarsens a little with increasing temperature toward the growth process of the  $\beta$ -Zr phase.

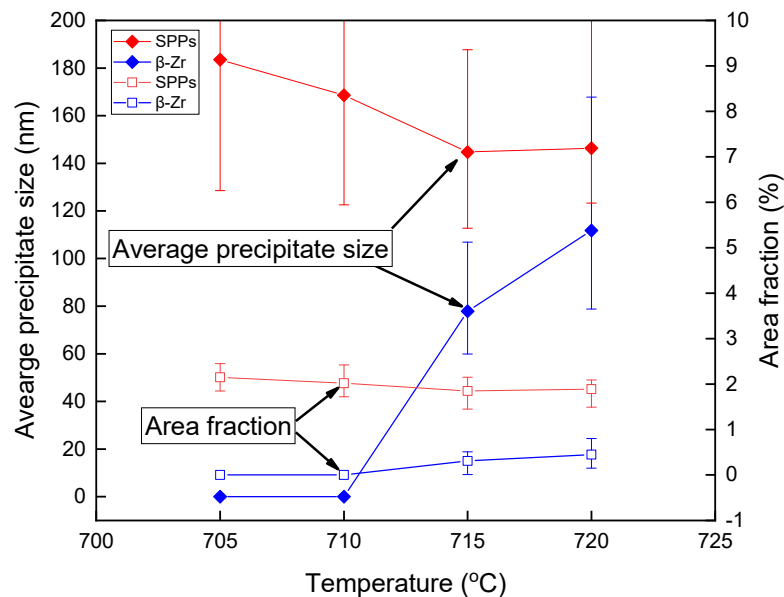


**Figure 7.** Statistical results of  $\beta$ -Zr and SPPs represented by area fraction evolution and precipitates size.

It is noteworthy that Nikulina et al. [23] found the phase transition temperature is about 650 °C in Zr-1% Sn-1% Nb-0.4%Fe alloy, and a temperature of 680 °C is reported by Zhao et al. [18] in N36 zirconium alloy. Both results were obtained by using the metallography method initially in a fully re-crystallized state. These temperatures are significantly lower than that of the metallographic results in the current study, which is significantly higher between 710–715 °C. According to the effect of alloying elements on phase stability, Nb and Fe are known as a  $\beta$ -phase stabilizer, due to limited solid solubility in  $\alpha$ -phase and vice versa in  $\beta$ -phase, while, Sn generally agreed to be  $\alpha$ -phase stabilizer [33,34]. It is important to note that only Sn has a significant difference of alloy content compared to that used by [18,23]. Therefore, it is probable that the difference in the initial transition temperature is result of the current study as compared with Zhao [18] and Nikulina [23], due to the possibility of Sn to behave as stabilizing factor for  $\alpha$ -phase. However, the result was the opposite of what was expected.

Regarding the effect of the initial material state, the discharge of energy at grain boundaries and the diffusion of alloying elements are both known to be desirable for  $\beta$ -Zr to nucleate and grow. Therefore, during the heating of the re-crystallized materials, the process of the dissolution and transition of precipitates to a new phase will be smoother due to the absence of obstacles, and the growth process of  $\beta$ -Zr will be concentrated at the grain boundaries. During the heating of  $\beta$ -quenched material, a conflict between the pressure driving force of recrystallization proceeding and the zener pinning effect generated from SPPs would occur [35]. Therefore, strain induced boundary migration tries to induced re-crystallization in  $\alpha$ -plates structure [36]. In contrast, the SPPs try to hinder the re-crystallization movement, especially in the sites that have coarser SPPs, until a high temperature is reached to overcomes these obstacles and smooth the re-crystallization process, SPPs dissolution, and forming a new phase.

Regarding the difference between DSC and metallographic results, it is known that it is difficult to reach an ideal thermal equilibrium condition during the heating process in a solid state, and thus, this will affect the diffusion rate [37]. Therefore, such a difference in the results is due to the non-equilibrium conditions during the normal heating rate in DSC.

#### 4. Conclusions

Dynamic and metallographic techniques were employed in the process of attaining the phase transition temperature in N36 zirconium alloy following  $\beta$ -quenching. The following key features were acquired:

1. In the current study, it has been verified that the phase transition temperature in  $\beta$ -quenched N36 zirconium alloy is 710–715 °C.
2. A peak separation of two endothermic peaks in the DSC curve enabled a successful study and explanation of SPPs dissolution and  $\alpha/\beta$  phase transformation.
3. Metallographic techniques represented by FEG-SEM and TEM successfully and precisely determined  $T_{\alpha \rightarrow \alpha+\beta}$  in  $\beta$ -quenched N36 zirconium alloy.
4. Compared to other documented papers concerning phase transition temperature in N36 zirconium alloy, the  $\beta$ -quenched starting material was responsible for delayed  $\beta$ -Zr formation in both methods.

**Author Contributions:** A.W.A.: methodology, Validation, Formal analysis, Visualization, Writing—original draft, review & editing, Z.C.: Review, Revision, Format revision, Article structure construction. I.A.D.: Review & editing. K.Y.: Resources. Y.Z.: Resources. All authors have read and agreed to the published version of the manuscript.

**Funding:** This research received no external funding. The APC pay by the first author.

**Data Availability Statement:** The Fundamental Research Funds for the Central Universities of NPU (3102019GHXM002), and Advanced Materials Characterization Institute (AMCI) School of Metallurgy and Materials Engineering University of Tehran.

**Acknowledgments:** The authors gratefully acknowledge financial support from National Key R&D Program of China (NO.2018YFB1900100). The authors gratefully acknowledge the Nuclear Power Institute of China for the N36 Zr alloy plate.

**Conflicts of Interest:** The authors declare that they have no competing interest.

#### References

1. Liu, W.; Li, Q.; Zhou, B.; Yan, Q.; Yao, M. Effect of heat treatment on the microstructure and corrosion resistance of a Zr–Sn–Nb–Fe–Cr alloy. *J. Nucl. Mater.* **2005**, *341*, 97–102. [[CrossRef](#)]
2. Meiyi, Y.; Bangxin, Z.; Qiang, L.; Wenqing, L.; Yuliang, C. A single-specimen-method for investigating effect of alloying composition on corrosion resistance of zirconium alloys. *RARE Met. Mater. Eng.* **2006**, *35*, 1651–1655.
3. Chen, L.; Li, J.; Zhang, Y.; Lu, W.; Zhang, L.; Wang, L.; Zhang, D. Effect of low-temperature pre-deformation on precipitation behavior and microstructure of a Zr–Sn–Nb–Fe–Cu–O alloy during fabrication. *J. Nucl. Sci. Technol.* **2016**, *53*, 496–507. [[CrossRef](#)]
4. He, G.; Liu, J.; Li, K.; Hu, J.; Mir, A.H.; Lozano-Perez, S.; Grovenor, C. Investigating the stability of second phase particles in Zr–Nb alloys under irradiation. *J. Nucl. Mater.* **2019**, *526*, 151738. [[CrossRef](#)]
5. Kim, J.H.; Lee, M.H.; Choi, B.K.; Jeong, Y.H. Effect of the hydrogen contents on the circumferential mechanical properties of zirconium alloy claddings. *J. Alloy. Compd.* **2007**, *431*, 155–161. [[CrossRef](#)]
6. Fan, Q.; Yuan, B.; Xie, M.; Shi, M.; Zhou, J.; Yang, Z.; Zhao, W. Effects of hot rolling temperature and aging on the second phase particles of Zr–Sn–Nb–Fe zirconium alloy. *Nucl. Mater. Energy* **2019**, *20*, 100700. [[CrossRef](#)]
7. Sun, C.; Yang, Z.; Wu, Z. Study on Corrosion Resistance of N36 Zirconium Alloy in LiOH Aqueous Solution. *World J. Nucl. Sci. Technol.* **2018**, *8*, 30–37. [[CrossRef](#)]
8. Chen, L.; Song, X.; Pang, H.; Liu, L. Influence of second phase particles on corrosion resistance of N36 alloy in superheated steam. *Prog. Nucl. Energy* **2016**, *93*, 84–88. [[CrossRef](#)]
9. Chai, L.; Luan, B.; Gao, S.; Chen, J.; Liu, Q. Study of precipitate evolution and recrystallization of  $\beta$ -quenched Zr–Sn–Nb–Fe–Cr–Cu alloy during aging. *J. Nucl. Mater.* **2012**, *427*, 274–281. [[CrossRef](#)]
10. Liu, Y.Z.; Zhao, W.J.; Peng, Q.; Jiang, H.M.; Zu, X.T. Study of microstructure of Zr–Sn–Nb–Fe–Cr alloy in the temperature range of 750–820 C. *Mater. Chem. Phys.* **2008**, *107*, 534–540. [[CrossRef](#)]
11. Dupin, N.; Ansara, I.; Servant, C.; Toffolon, C.; Lemaignan, C.; Brachet, J. A thermodynamic database for zirconium alloys. *J. Nucl. Mater.* **1999**, *275*, 287–295. [[CrossRef](#)]



12. Qiu, R.; Luan, B.; Chai, L.; Zhang, X.; Liu, Q. Effects of heating rates and alloying elements (Sn, Cu and Cr) on the  $\alpha \rightarrow \alpha + \beta$  phase transformation of Zr–Sn–Nb–Fe–(Cu, Cr) alloys. *J. Nucl. Mater.* **2014**, *453*, 269–274. [[CrossRef](#)]
13. Corchia, M.; Righini, F. Kinetic aspects of the phase transformations in zircaloy-2. *J. Nucl. Mater.* **1981**, *97*, 137–148. [[CrossRef](#)]
14. Qiu, R.; Luan, B.; Chai, L.; Zhang, X.; Liu, Q. Precise determination of the  $\alpha \rightarrow \alpha + \beta$  phase transformation temperature of Zr-1.0Sn-0.3Nb-0.3Fe alloy. *Sci. China Technol. Sci.* **2012**, *56*, 60–65. [[CrossRef](#)]
15. Canay, M.; Danon, C.A.; Arias, D. Phase transition temperature in the Zr-rich corner of Zr–Nb–Sn–Fe alloys. *J. Nucl. Mater.* **2000**, *280*, 365–371. [[CrossRef](#)]
16. Curtis, R.E.; Dressler, G. Effect of Thermomechanical Processing. In *Zirconium in Nuclear Applications: A Symposium Co-sponsored by the American Society for Testing and Materials and the American Institute of Mining, Metallurgical, and Petroleum Engineers, 21–24 August 1973, Portland, OR, USA; American Society for Testing and Materials: West Conshohocken, PA, USA, 1974*; p. 104.
17. Baifeng, L.; Jing, S.; Tianlin, H.; Jun, Z.; Xiyan, Z.; Qing, L. Effect of Sn Content on Phase Transformation Temperature and Precipitation of Zr–Sn–Nb–Fe–Cr Zirconium Alloy. *Rare Met. Mater. Eng.* **2012**, *41*, 830–834.
18. Zhao, W.; Liu, Y.; Jiang, H.; Peng, Q. Effect of heat treatment and Nb and H contents on the phase transformation of N18 and N36 zirconium alloys. *J. Alloy. Compd.* **2008**, *462*, 103–108. [[CrossRef](#)]
19. Ma, H.Z.; Zhai, T.D.; Shi, K.X.; Zhang, J.; Sun, X.F.; Hou, X.Y. Determination of phase transformation temperatures of Zr–Sn and Zr–Nb zircalloys by metallographic method. *Phys. Test. Chem. Anal. Part A (Phys. Test.)* **2018**, *54*, 115–118.
20. Massih, A.R.; Jernkvist, L.O. Solid state phase transformation kinetics in Zr-base alloys. *Sci. Rep.* **2021**, *11*, 1–16. [[CrossRef](#)]
21. Motta, A.; Faldowski, J.; Howe, L.; Okamoto, P. In Situ Studies of Phase Transformations in Zirconium Alloys and Compounds Under Irradiation. *ASTM Spec. Tech. Publ.* **1996**, *1295*, 557. [[CrossRef](#)]
22. Kobylansky, G.P.; Novoselov, A.E.; Obukhov, A.V.; Ostrovsky, Z.E.; Shishov, V.N.; Peregud, M.M.; Markelov, V.A.; Barberis, P.; Dean, S.W. Radiation Damage of E635 Alloy Under High Dose Irradiation in the VVER-1000 and BOR-60 Reactors. *J. ASTM Int.* **2011**, *8*, 1–14. [[CrossRef](#)]
23. Nikulina, A.; Markelov, V.; Peregud, M.; Voevodin, V.; Panchenko, V.; Kobylansky, G. Irradiation-induced microstructural changes in Zr-1% Sn-1% Nb-0.4% Fe. *J. Nucl. Mater.* **1996**, *238*, 205–210. [[CrossRef](#)]
24. Burgers, W. On the process of transition of the cubic-body-centered modification into the hexagonal-close-packed modification of zirconium. *Physica* **1934**, *1*, 561–586. [[CrossRef](#)]
25. Aldeen, A.W.; Chen, Z.W.; Disher, I.A.; Zhu, Y.; Yan, K. Growth Kinetics of Second Phase Particles in N36 Zirconium Alloy: Zr–Sn–Nb–Fe. *J. Mater. Res. Technol.* **2022**, *17*, 2038–2046. [[CrossRef](#)]
26. Mizuhata, M.; Sumihiro, Y.; Deki, S. Structure and the conductive behaviour of hydrate melt coexisting with porous solid materials— $\alpha$ -Al<sub>2</sub>O<sub>3</sub> powder/ZnCl<sub>2</sub> hydrate melt coexisting system. *Phys. Chem. Chem. Phys.* **2004**, *6*, 1944–1951. [[CrossRef](#)]
27. Hong-Wang, Y.; Wei-Ping, T.; Xiang, Z.; Liang, Z.; Jian-Qiang, W. Observation of  $\beta$ -Relaxation in Sub- $T_g$  Isothermally Annealed Al-Based Metallic Glasses. *Chin. Phys. Lett.* **2008**, *25*, 3357–3359. [[CrossRef](#)]
28. Riontino, G.; Massazza, M.; Lussana, D.; Mengucci, P.; Barucca, G.; Ferragut, R. A novel thermal treatment on a Mg–4.2Y–2.3Nd–0.6Zr (WE43) alloy. *Mater. Sci. Eng. A* **2008**, *494*, 445–448. [[CrossRef](#)]
29. Arias, D.; Roberti, L. The solubility of tin in  $\alpha$  and  $\beta$  zirconium below 1000 °C. *J. Nucl. Mater.* **1983**, *118*, 143–149. [[CrossRef](#)]
30. Okamoto, H. Sn–Zr (Tin–Zirconium). *J. Phase Equilibria Diffus.* **2010**, *31*, 411–412. [[CrossRef](#)]
31. Liu, J.; He, G.; Callow, A.; Li, K.; Moore, K.L.; Nordin, H.; Moody, M.; Lozano-Perez, S.; Grovenor, C.R.M. The role of  $\beta$ -Zr in a Zr-2.5 Nb alloy during aqueous corrosion: A multi-technique study. *Acta. Mater.* **2021**, *215*, 117042. [[CrossRef](#)]
32. Harte, A.; Griffiths, M.; Preuss, M. The characterisation of second phases in the Zr–Nb and Zr–Nb–Sn–Fe alloys: A critical review. *J. Nucl. Mater.* **2018**, *505*, 227–239. [[CrossRef](#)]
33. Woo, O.; Griffiths, M. The role of Fe on the solubility of Nb in  $\alpha$ -Zr. *J. Nucl. Mater.* **2009**, *384*, 77–80. [[CrossRef](#)]
34. Charquet, D.; Hahn, R.; Ortlieb, E.; Gros, J.-P.; Wadier, J.-F. *Solubility Limits and Formation of Intermetallic Precipitates in ZrSnFeCr Alloys*; ASTM International: West Conshohocken, PA, USA, 1989.
35. Humphreys, F.J.; Hatherly, M. *Recrystallization and Related Annealing Phenomena*; Elsevier Science Ltd.: Oxford, UK, 2012.
36. Rumball, W.; Coleman, C. Massive grain growth during aging of quenched Zr/1.25 wt% Cr/0.1 wt% Fe. *J. Nucl. Mater.* **1970**, *36*, 147–152. [[CrossRef](#)]
37. Zhu, Y.T.; Lowe, T.C. Application of, and precautions for the use of, the Rule of additivity in phase transformation. *Met. Mater. Trans. A* **2000**, *31*, 675–682. [[CrossRef](#)]